Effects of Porous Parameters on the Aerodynamic Noise of the Blowing Device of Guardrails

M. H. Zhang[†] and H. J. Shi

Department of Mechanical and Electronic Engineering, Shandong University of Science and Technology, Qingdao, 266590, China

†*Corresponding Author Email: m.h.zhang@sdust.edu*

ABSTRACT

To solve the problem of the strong noise generated in the galvanizing process on the surface of the guardrail board, optimal design of the outlet structure of the blowing device is carried out according to the sound absorption and noise reduction theory of microperforated plates. The aerodynamic characteristics and aerodynamic noise analysis of the blowing device are investigated by large eddy simulation with dynamic grid technology. The oblique surface of the outlet is processed with blind holes, and then the influence of blind holes on the aerodynamic noise of the blowing device is explored, including different shapes, porosities and depths. The spectral study reveals that when the guardrail board just enters the blowing device, there is greater noise compared to other working conditions. The place with the highest noise sound pressure level (SPL) is at the outlet of the blowing device at the monitoring point of R=1 m and the direction of 90°. The SPLs of the monitoring points at 0° and 180° are smaller than those in other directions, while the SPL distribution of the monitoring points in other directions is relatively even. Compared with the original blowing device, the best noise reduction performance is achieved when the blowing device has cylindrical holes, with a porosity of 10% and a hole depth of 3 mm. The noise reduction value reaches up to 28.4 dB. In addition, an aerodynamic noise test was carried out on the blowing device in the corrugated board galvanizing workshop to demonstrate the correctness of the results of the numerical simulation.

Keywords: Blowing device; Impinging jet; Aerodynamic noise; Porous parameters; Brand noise reduction.

NOMENCLATURE

d_h	depth of the hole	a	far-field sound velocity
h_c	centroid distance between two adjacent holes in each row	p	sound pressure at the observation point
N_h	number of holes in each row	p_1	instantaneous sound pressure
t_c	circumferential distance between two adjacent rows of holes	u_i	x_i-direction velocity component
R_w	rows of holes along the circumference of the outlet	u_n	fluid velocity perpendicular to the integral surface
σ	porosity of the hole	v_n	moving speed component of the integral surface
A_{pore}	cumulative area of the blind holes	T_{ij}	Lighthill tensor
A_{total}	total area of the inclined surface of the outlet of the core mold	P_{ij}	stress tensor
τ_{ij}	subgrid scale Reynolds stress		

1. INTRODUCTION

Corrugated board (shown in Fig. 1), as the protective guardrail on both sides of the highway, plays a vital role in exerting the efficiency of the highway, preventing and reducing the occurrence of traffic accidents. To improve the service life of corrugated plates in harsh environments, hot-dip galvanizing processes are often used to treat the surface of the corrugated board, which can produce an anticorrosive layer. After galvanizing is completed, the excess zinc particles on the surface of the
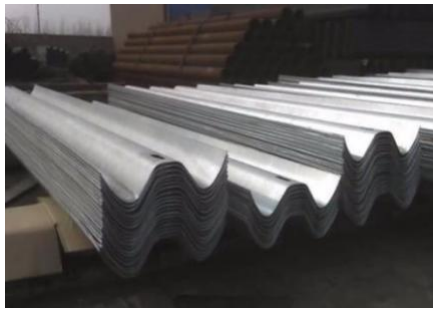
Fig. 1. Guardrail board.

Fig. 2. Zinc particle blowing site (1-Fork, 2-Rotating roller, 3-Blowing device, 4-Guardrail board, 5-Rotating fork, 6-Gas pipeline).

corrugated board have to be blown off by the blowing device. The zinc particle blowing site is shown in Fig. 2. After the guardrail comes out of the galvanizing pool, it is driven by the fork to move horizontally to the rotating roller. Under the rotation of the roller, the guardrail moves forward at a speed of 1 m/s and passes through the inside of the external blowing device. After blowing by the external blowing device, it is moved to the next process by the rotating fork. However, strong noise will be generated during the blowing process of zinc particles, and the noise sound pressure will be between 90 dB and 120 dB, which will seriously endanger the health of workshop staff and surrounding residents. Consequently, it is important to analyze the noise mechanism of the original blowing device model and find a way to reduce its aerodynamic noise based on this.

The source of strong noise generated by blowing off zinc particles on the surface of the guardrail board is mainly the aerodynamic noise generated when the blowing device ejects high-speed air, which is jet noise. Currently, there is much research on jet noise. In terms of theoretical research on jet noise, Ilário *et al.* (2017) presented a computational aeroacoustics prediction tool to compute noise from subsonic turbulent jets based on the application of Lighthill's theory. Both the source model and the refraction model are used to collect flow information from a solution of the Reynolds-averaged Navier–Stokes equations. Pankaj and Sunil (2019) investigated the aerodynamic and acoustic features under the interaction of a nozzle injector with the main jet using large eddy simulations. Semiletov *et al.* (2016) conducted integrated large eddy simulations (MILES) based on the CABARET scheme for a coaxial subsonic unheated jet with and without a swept lifting wing under free-stream conditions. Viswanathan (2018) developed a new method to

predict the noise of realistic dual-stream jets. The main purpose of this method is to gain better quantification and understand the nonjet noise components. Semiletov and Karabasov (2017) implemented a new low-order noise prediction scheme based on the Goldstein generalized acoustic analogy. A static isothermal jet is calculated using the large eddy simulation database of fluctuating Reynolds stress fields. Tester and Glegg (2018) reviewed the basis of beamformer and polar correlation phased array methods and showed that these methods provide different information about axially distributed, noncompact noise sources. Lee *et al.* (2017) carried out an acoustic analogy analysis based on a decomposition of the source term in Lighthill's equation for a subsonic turbulent jet exhausting from a baseline round nozzle. Bychkova and Faranosov (2014) proposed a qualitative model of the jet noise enhancement mechanism emanating from nozzles located near the wing and found that diffraction on the wing edge of Kelvin–Helmholtz instability waves developing from the edge of the nozzle can lead to the intensification of the acoustic energy radiated into the far field. Nelson *et al.* (2017) applied the synthetic array technique to diagnose the source of unexpected (and nonphysical) tones that arose in unsteady computational fluid dynamics (CFD) simulations of hot supersonic jets. Shur *et al.* (2016) performed jet noise computations using detached eddy simulation and the Spalart-Allmaras model. Liu (2016) proposed suppressing the jet noise of stationary chevron nozzle exits through unsteady excitation of secondary instabilities. Brehma *et al.* (2017) studied the noise-generating mechanism for four direct-impact supersonic jets using implicit large eddy simulations. Karabasov and Sandberg (2015) imitated sound generation and propagation by low-Reynolds number turbulent jets from a DNS database. Liu *et al.* (2014) established a method of combining large eddy simulation (LES) and Lighthill's acoustic analogy theory to compute the hydrodynamic noise. Pouangué *et al.* (2015) found that using fully tetrahedral grids can provide a way to interpret complex noise-reduction devices such as chevrons, realistic dual-stream nozzles, or lobed mixers. Barbarino *et al.* (2017) proposed an active fluid injection technique based on extractions and injections of high-pressure gas into the main stream of exhaust through the mixing and breaking of turbulent eddies. Baqui *et al.* (2015) investigated source mechanisms for subsonic jet noise using experimentally obtained datasets of high-Reynolds-number Mach 0.4 and 0.6 turbulent jets.

In terms of experimental research on jet noise, Dahl (2015) studied the influence of filtering on the statistical properties of the velocity fluctuations relevant to jet noise prediction modeling. Faranosov and Belyaev (2019) conducted an experimental study at subsonic Mach numbers (up to 0.82) for the configuration in which the plate trailing edge is located in the linear hydrodynamic jet near field. Anyoji and Tabaru (2017) investigated the characteristics of transonic resonance and tones using a circular C-D nozzle and evaluated the effects of the boundary layer trip using a tripping wire. Balakrishnan and Srinivasan (2017) carried out

experimental work on the acoustic far field and flow field characteristics of confined coaxial swirling pipe jets. Wei *et al.* (2019) conducted an experimental investigation into noise reduction of supersonic jets through nozzle trailing-edge modifications, whereby far-field acoustic measurements were captured for two different stepped nozzles under two distinct under-expanded conditions. Baskaran *et al.* (2018) investigated the effect of passive grids on the acoustic characteristics of pipe and orifice jets for different nozzle pressure ratios. Koenig *et al.* (2016) presented the turbulent and acoustic fields of subsonic jets controlled by means of a novel actuator. Balakrishnan and Srinivasan (2019) carried out experimental studies in the acoustic far field and flow visualization on circular and noncircular impinging jets at a nozzle-to-plate distance ratio of 5. Pilon *et al.* (2017) described an active control device that deflects a fraction of the adjustable seals in the divergent section of the engine exhaust nozzle. Lee *et al.* (2019) researched the noise characteristics of a dual-stream jet with bypass ratios greater than 10 in response to the area ratio, nozzle operating conditions, installation effect, and chevron effect. Doty *et al.* (2018) described jet noise measurements from a hybrid wing body acoustic test in the NASA Langley 14- by 22-Foot Subsonic Tunnel. Both an axisymmetric and low noise chevron nozzle set are investigated in the context of shielding.

In previous studies, the researchers focused on the characteristic analysis of the flow field and sound field and the research on the noise reduction mechanism for round or square nozzles. This type of nozzle has a simple structure, and the position of the object to be blown off is fixed, or the ejected gas is directly discharged into the atmosphere. There are few studies on jets with moving object boundaries, especially for complex structures such as blowing devices of guardrails. As part of efforts to fill the knowledge gap, taking the external blowing device of the corrugated board as the research object, dynamic grid technology is introduced into the aerodynamic characteristics and aerodynamic noise analysis of the external blowing device. The changing law of the flow field parameters inside the cavity of the external blowing device and around the guardrail and the far pressure sound field are discussed when the guardrail is moving. In addition, the blind hole treatment is carried out on the oblique surface of the core mold outlet of the external blowing device according to the sound absorption and noise reduction theory of microperforated plates. The influence of different shapes, porosities and depths of blind holes on aerodynamic noise is explored. In this paper, we have focused on the following areas: (1) The changing law of the flow field parameters inside the cavity of the blowing device and around the guardrail during the movement of the guardrail is studied based on dynamic grid technology. (2) The SPL distribution inside the cavity of the blowing device and the guardrail surface is studied by performing broadband noise analysis. The noise source with the largest sound pressure level is identified. (3) The influence of different shapes, porosities and depths of blind holes on aerodynamic noise is explored. (4) The

noise of certain monitoring points in the corrugated board hot-dip galvanizing workshop is collected and measured to verify the correctness of the numerical simulation results.

The rest of this article is arranged as follows: the next section briefly reviews the blowing device models in detail, including the structure of the external blowing device, the position of the blind hole and the related parameters of the blind hole. Next, the fundamentals of the numerical simulation, grid topology and boundary conditions are given. This is followed by the section in which the results of the numerical simulation are presented and discussed. Then, experimental schemes and experimental results are proposed and discussed. Finally, the results of this study are summarized.

2. BLOWING DEVICE MODELS

The present article aims to investigate the flow field parameters and SPL distribution inside the cavity of the original blowing device and the guardrail surface by exploring the influence of different shapes, porosities and depths of blind holes on aerodynamic noise. The blowing device, with a nominal width w =474 mm, a nominal height h=240 mm and a nominal thickness t_h=71 mm, is composed of a front board, a rear cover, a support frame and a core mold. To ensure that the excess zinc particles on the guardrail board are blown evenly, the core mold of the blowing device is designed to have the same wave shape as the guardrail board. 3D modeling of the blowing device is shown in Fig. 3. Two inlets are provided on the upper and lower surfaces of the blowing device. The distance between the nozzle outlet of the blowing device and the surface of the guardrail board is 4 mm.
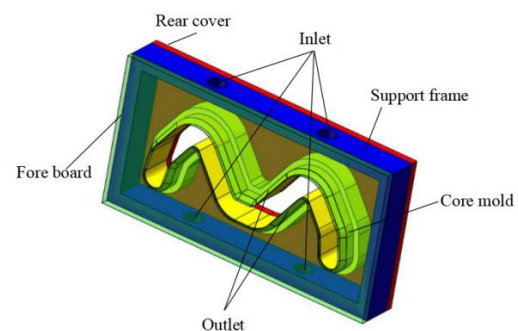

Fig. 3. 3D modeling of the blowing device.

To improve the gas state at the outlet of the blowing device, reduce the degree of turbulence and reduce aerodynamic noise, a large number of core molds with blind holes are investigated in this study. These molds have different blind hole shapes and combinations of the porosity and depth of the blind hole to compare the aeroacoustics performance of the blow device between the original core mold and the porous core molds. The blow device with the original core mold is calculated by numerical simulation under the same flow conditions as the blow devices with porous core molds. The specific parameters of these porous core molds are summarized in Tables 1–

3. Regarding the symbols in the t, for round holes, d represents the diameter of the hole; for square holes or triangular holes, d indicates the side length of the hole. d_h represents the depth of the hole, h_c is the centroid distance between two adjacent holes in each row, and N_h is the number of holes in each row. t_c is the circumferential distance between two adjacent rows of holes, R_w is the rows of holes along the circumference of the outlet, and σ represents the porosity of the hole.

In the first set of numerical simulations, to research the noise of blow devices with different shapes of blind holes, one original core mold and three porous core mold structures were used in acoustic numerical simulations. The blind holes are arranged on the inclined surface of the outlet of the core mold, with 5 holes in each row, and several rows are arranged along the circumference of the outlet. The porosity of the blind holes is σ=5%. The distribution of blind holes is shown in Fig. 4(a). The shapes of the blind holes are round holes, square holes and triangular holes, which are shown in Fig. 4(b). Affected by the width of the outlet ramp and processing factors, each row is provided with 5 blind holes, and a partially enlarged view of the blind hole is shown in Fig. 4(c). The geometrical parameters of the core molds investigated in this study are shown in Table 1.

The porosity σ is defined as:

$$\sigma = \frac{A_{pore}}{A_{total}} \tag{1}$$

where A_{pore} is the cumulative area of the blind holes and A_{total} is the total area of the inclined surface of the outlet of the core mold.

According to the numerical simulation results of the first series, the blind hole shape with the best noise reduction effect is determined. Based on this, the second set of numerical simulations focuses on the effect of the porosity on broadband noise in the far flow field. The levels of porosity are depicted in Table 2.

According to the numerical simulation results of the second series, we determine the porosity with the best noise reduction effect. Based on this, the third set of numerical simulations explores the influence of different depths of the hole on broadband noise in the far flow field. The core molds have the same hole shape and the same porosity. The parameters are shown in Table 3.
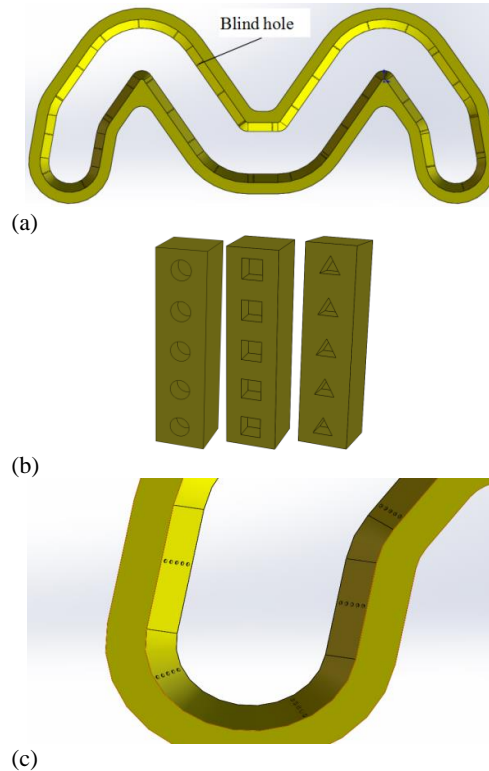

(a)

(b)

(c)

Fig. 4. (a) Distribution of blind holes, (b) the shapes of the blind holes, and (c) a partial enlarged view of a blind hole.

Table 1 Blind hole parameters with different shapes

Types of Hole	d(mm)	d_h(mm)	N_h	R_w	h_c(mm)	t_c(mm)	σ
Round	1	2	5	76	4	20.27	5%
Square	1	2	5	60	4	25.68	5%
Triangular	1	2	5	120	4	12.84	5%

Table 2 Blind hole parameters with different porosities

Types of Hole	d(mm)	d_h(mm)	N_h	R_w	h_c(mm)	t_c(mm)	σ
Round	1	2	5	76	4	20.27	5%
Round	1	2	5	152	4	10.14	10%
Round	1	2	5	228	4	6.76	15%
Round	1	2	5	304	4	5.07	20%

Table 3 Blind hole parameters with different depths

Types of Hole	d(mm)	d_h(mm)	N_h	R_w	h_c(mm)	t_c(mm)	σ
Round	1	1	5	152	4	10.14	10%
Round	1	2	5	152	4	10.14	10%
Round	1	3	5	152	4	10.14	10%
Round	1	4	5	152	4	10.14	10%

3. COMPUTATIONAL SETUP

3.1 Aerodynamic Computation

In this decade, large eddy simulations have become the primary tool for studying jet noise sources due to their inherent ability to capture broadband turbulent features.

The filtering speed is as follows:

$$\overline{u_i}(x,t) = \int G(x,x',\Delta) u_i(x',t) dx' \qquad (2)$$

where $\int G(x,x',\Delta)$ is the filtering function; here, $G(x) = \sqrt{6/\pi}(1/\Delta)\exp\left[-6(x-x')^2/\Delta^2\right]$, $u_i(x',t)$ represents a small-scale amount, and $\overline{u_i}(x,t)$ represents the large-scale average amount.

The N-S equation can be rewritten as:

$$\frac{\partial \rho}{\partial t} + \frac{\partial}{\partial x_i}(\rho \overline{u_i}) = 0 \qquad (3)$$

$$\frac{\partial \rho \overline{u_i}}{\partial t} + \frac{\partial \rho \overline{u_i} \overline{u_j}}{\partial x_j} = -\frac{\partial \overline{p}}{\partial x_i} + \frac{\partial}{\partial x_j}\left[u\left(\frac{\partial \overline{u_i}}{\partial x_j} + \frac{\partial \overline{u_j}}{\partial x_i}\right)\right] - \frac{\partial \rho(\overline{u_i u_j} - \overline{u_i}\,\overline{u_j})}{\partial x_j}$$

$$= -\frac{\partial \overline{p}}{\partial x_i} + \frac{\partial}{\partial x_j}\left[\mu\left(\frac{\partial \overline{u_i}}{\partial x_j}\right) - \tau_{ij}\right] \qquad (4)$$

where τ_{ij} represents the subgrid-scale Reynolds stress, $\rho(\overline{u_i u_j} - \overline{u_i}\,\overline{u_j}) = \tau_{ij}$.

3.2 Governing Acoustic Analogy Equations

The sound source term is calculated through the unsteady flow field and then combined with the FW-H acoustic analogy equation to obtain the noise propagation characteristics of the jet flow in the blowing device of the corrugated plate. The control equation is as follows:

$$\frac{1}{a^2}\frac{\partial^2 p}{\partial t^2} - \nabla^2 p = \frac{\partial^2}{\partial x_i y_i}\left\{T_{ij} H(f)\right\}$$
$$-\frac{\partial}{\partial x_i}\left\{\left[p_{ij} n_j + \rho u_i \left(u_n - v_n\right)\right]\delta(f)\right\} \qquad (5)$$
$$+\frac{\partial}{\partial t}\left\{\left[\rho_0 v_n + \rho\left(u_n - v_n\right)\right]\delta(f)\right\}$$

where a is the far-field sound velocity, p is the sound pressure at the observation point, $f=0$ is the integration surface of the sound source data, u_i is the x_i-direction velocity component, u_n is the fluid velocity perpendicular to the integral surface, v_n is the moving speed component of the integral surface, T_{ij} is the Lighthill tensor, P_{ij} is the stress tensor, $H(f)$ is the Heaviside function, and $\delta(f)$ is the Dirac function.

The SPL can be calculated at a far-field location as follows:

$$SPL = 20 \times \lg\left(\frac{p_1}{p_{ref}}\right), (dB) \qquad (6)$$

where p_1 is the instantaneous sound pressure and $p_{ref} = 2\times10^{-5}$ Pa, is the reference pressure.

3.3 Grid Topology and Boundary Conditions

Grid division is very important for numerical simulation calculations. When dividing the grid, it is essential to examine the influence of the number of grids on the accuracy of the numerical calculation results and the impact of the number of grids on the calculation time. For the blowing device, its structure is very complicated. If a structured grid is used, the division of the grid is very cumbersome. Therefore, in this paper, unstructured tetrahedral grids are used to divide the blowing device and its external flow field. The coordinate system of the calculation area is denoted by *X*, *Y* and *Z*, which refer to the corrugated board width direction, corrugated board thickness direction and the direction of corrugated board movement, respectively. It should be noted that *Z* = 0 is located at the back end of the corrugated board when *t*=0. The corrugated board moves along the negative direction of the *Z* axis. This coordinate system is employed throughout the paper. Since the movement of the corrugated plate will affect the outlet flow field and aerodynamic noise of the external blowing device, the computational domain consists of five parts: (1) the area of the corrugated plate close to the external blowing device, (2) the area of gas injection, (3) the area of the external blowing device, (4) the area of gas injection, and (5) the area where the corrugated plate leaves the blowing device. The size of the calculation area is determined by the injection distance of the gas at the outlet of the external blowing device and the size of the corrugated plate.

The entire flow field area along the *X*, *Y*, and *Z* axes is 600 mm×400 mm×2200 mm. The grid of the entire flow field of the blowing device is shown in Fig. 5(a), and the grid of the internal flow field of the blowing device is shown in Fig. 5(b). Since the uppermost inclined surface of the core mold is at the outlet of the blowing device, where the high-speed gas flows through, a fine mesh should be used. The grid of the core mold and partial enlargement of blind hole mesh is shown in Fig. 5(c), while the grid of the guardrail board is shown in Fig. 5(d). It should be noted that the real length of the guardrail is 4320 mm, the width is 310 mm, and the height is 85 mm; however, the length of the guardrail used in the numerical simulation is 864 mm, and the width and height are the same size as those of the real guardrail. This is because the part of the corrugated board far away from the blowing device has less effect on the flow field and sound field. Moreover, the number of meshes to be divided is limited by computer memory and computing time. It was found that the numerical calculation results with this length of the guardrail are not much different from field test values.

Due to the continuous movement of the corrugated plate in the calculation process, the mesh around the corrugated plate should be redivided to ensure the accuracy of the calculation results. Since the moving
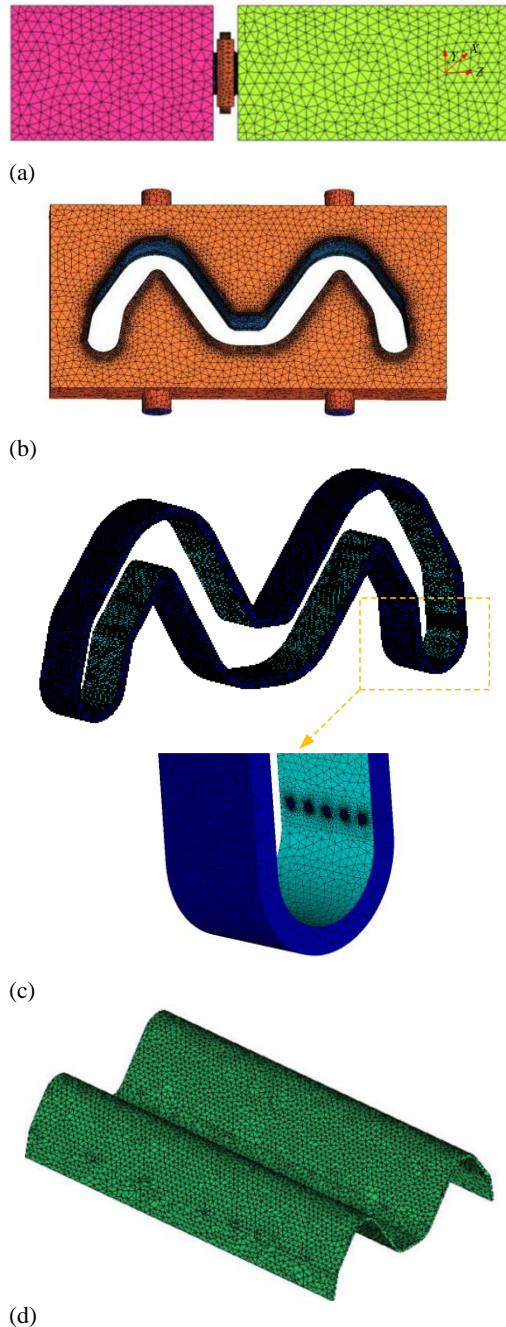
(a)

(b)

(c)

(d)

Fig. 5. (a) Grid of the entire flow field of the blowing device, (b) the grid of the internal flow field of the blowing device, (c) the grid of the core mold inclined plane, and (d) the mesh of the guardrail board.

boundary of the corrugated plate is much larger than the mesh size, the local redistricting model is adopted in this manuscript. That is, in the calculation process, if the mesh distortion rate is too large or the mesh size changes too violently, the mesh around the corrugated plate is redivided.

The entrance of the computational domain is set as the pressure inlet, and the exit is set as the pressure outlet. The other boundaries of the computational domain are set as wall conditions. The setting parameters of the boundary conditions are shown in Table 4.

Table 4 Boundary condition setting

The boundary of computational domain	Boundary condition setting
Inlet	p_{in}=0.3 MPa
Outlet	p_{out}=0
The others boundary	wall

3.4 Grid Independence Verification

The number of grids in the computational domain affects the accuracy and the duration of the simulation process. To evaluate the grid independence on the calculated results, seven different grid densities defined as the total number of grid nodes, including 2.32×10^6, 3.17×10^6, 4.46×10^6, 5.29×10^6, 6.18×10^6 and 7.24×10^6, are calculated for the original external blowing device without a guardrail board. In this paper, FLUENT software is used to calculate the flow field and aerodynamic noise. The sound pressure at the center $(0, 0, 0)$ of the blowing device for different grid numbers is shown in Fig. 6. It is shown that the noise value gradually increases as the number of grids increases when the number of grids is below 4×10^6. This is because the number of grids is too small and the volume of the element is too large to capture all pressure fluctuations in the flow field. When the number of grids is higher than 4×10^6, the discrepancies of the sound pressure value at the monitoring point fluctuate slightly, and the rate of change of the sound pressure value is within 0.8%. For efficient use of time, the numerical grid scheme pertaining to 5.29×10^6 is selected throughout this study.
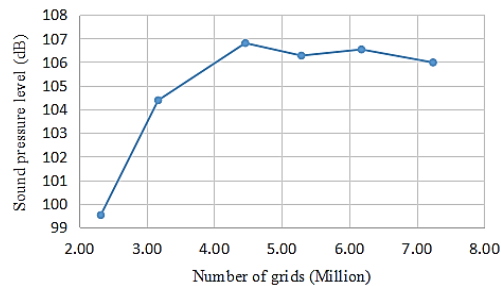

Fig. 6. Noise line chart of monitoring points at the center of the nozzle with different mesh numbers.

4. RESULTS AND DISCUSSION

4.1 Research on the Aerodynamic Noise of the Original Blowing Device

In this section, large eddy simulation is employed to perform transient flow field calculations for the original blowing device to obtain aerodynamic characteristics in the cavity and external flow field when the corrugated board moves. The aerodynamic noise of the blowing device is analyzed by combining the FW-H equation. The spectrum characteristics and the location of the largest sound pressure source are determined. This research work provides a theoretical basis that can guide the noise reduction design of blowing devices.
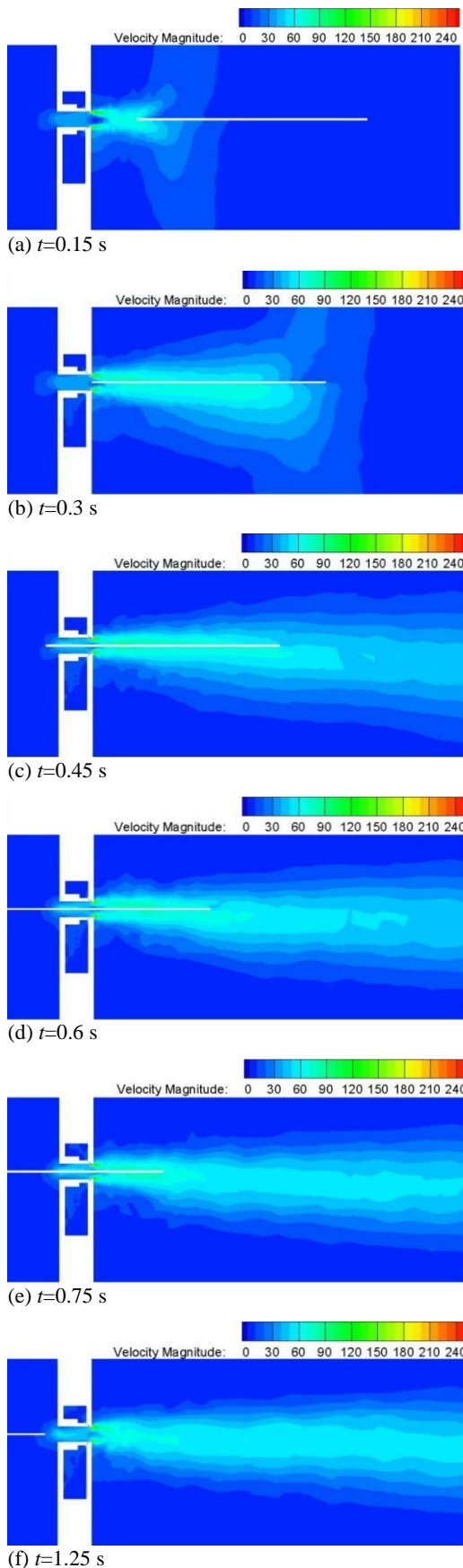
(a) *t*=0.15 s

(b) *t*=0.3 s

(c) *t*=0.45 s

(d) *t*=0.6 s

(e) *t*=0.75 s

(f) *t*=1.25 s

Fig. 7. Velocity contours of the *YZ* section at different times.

When the guardrail moves at the speed *v*=1 m/s, the velocity contours of the *YZ* section are shown in Fig. 7, where the center of the blowing device is located, with the time t=0.15 s (shown in Fig. 7(a)), 0.3 s (shown in Fig. 7(b)), 0.45 s (shown in Fig. 7(c)), 0.6 s (shown in Fig. 7(d)), 0.75 s (shown in Fig. 7(e)), and 1.25 s (shown in Fig. 7(f)). It is shown that the flow velocity increases rapidly after the air passes through the slits of the blowing device outlet. The high-velocity gas near the outlet impacts itself and drives the surrounding air to produce many disorderly eddies. The vortex area is divided into upper and lower parts with the movement of the guardrail. The vortex area converges again at the rear of the guardrail. These vortices propagate into the atmosphere at a certain speed to form a high-speed vortex area in the external flow field. The generation and diffusion of the vortex and the interaction between the vortices will produce pressure pulsation in the flow field outside the blowing device, which will generate aerodynamic noise.

The acoustic power level distribution for the blowing device and the surface of the guardrail during the movement of the guardrail are shown in Fig. 8. When the guardrail does not enter the blowing device, the acoustic power level distributions are shown in Fig. 8(a). When the guardrail just entered the blowing device, the acoustic power level distributions are shown in Fig. 8(b). When the guardrail enters halfway, the acoustic power level distributions are shown in Fig. 8(c). When the guardrail just exits, the acoustic power level distributions are shown in Fig. 8(d). It is shown that the sound pressure of the inlet, inner cavity of the blowing device and guardrail surface are relatively small, all less than 80 dB. The place with the largest noise SPL is at the outlet of the blowing device, and the SPL is above 120 dB. When the guardrail board just enters the blowing device, there is greater noise at the outlet than in other working conditions. This is because the guardrail board interacts with the high-intensity vortex at the outlet, which intensifies the turbulent pulsation intensity and produces greater pressure pulsation.

Through the sound field analysis of the blowing device, it is shown that the place with the largest sound pressure level is mainly located at the outlet, where turbulent pulsation is violent. The aerodynamic noise has obvious spatial directivity, and low-frequency noise is dominant. Therefore, we can optimize the outlet structure of the blowing device to improve the gas state of the outlet and reduce the turbulence pulsation intensity to reduce the aerodynamic noise of the blowing device.

4.2 Effect of Hole Shape on the Aerodynamic Noise of the Blowing Device

From the aerodynamic noise analysis of the original blowing device, it is shown that the place with the largest aerodynamic noise sound pressure level is mainly located at the outlet. Therefore, in this section, the optimal design of the outlet structure of the blowing device is carried out according to the sound absorption and noise reduction theory of microperforated plates. The oblique surface of the outlet is processed with blind holes to explore the
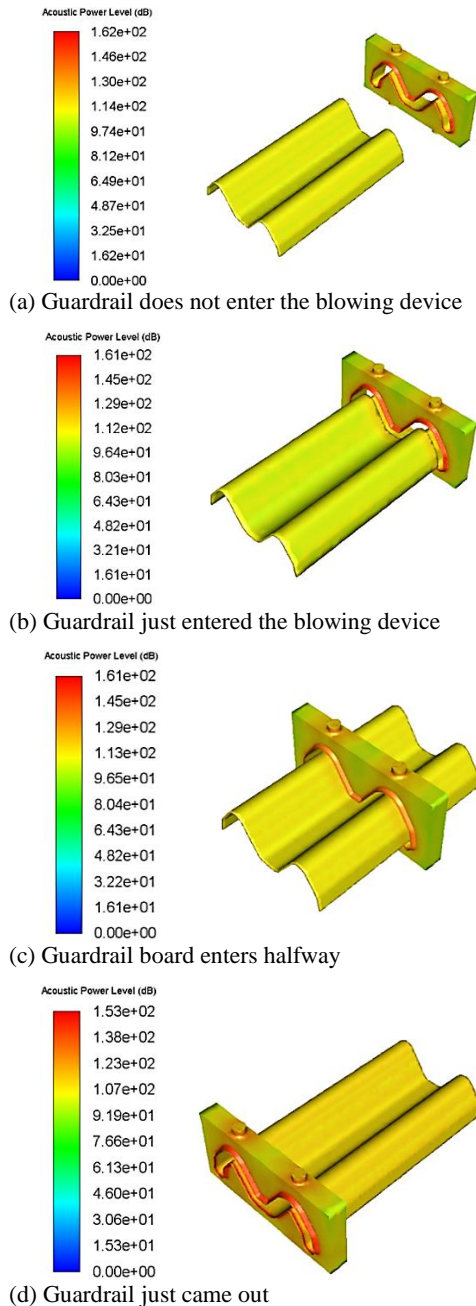
(a) Guardrail does not enter the blowing device

(b) Guardrail just entered the blowing device

(c) Guardrail board enters halfway

(d) Guardrail just came out

Fig. 8. Noise pressure level distribution on the surface of the blowing device and guardrail.

influence of different shapes of blind holes on the aerodynamic noise of the blowing device. Several rows of blind holes on the exit slope of the mandrel are drilled, 5 in each row, with a depth of 2 mm. The total area of the blind holes accounts for 5% of the slope area, as listed in Table 1. The variation in the SPL radiated from the blowing device with different shapes is investigated. Monitoring circles on the *XZ* plane are set up to monitor the SPL. The center of the external blowing device is the center of the circle, and 40 noise monitoring points are s*et al*ong the circumferential direction, with a radius of R=1, 3, 5, 7, and 9 m for each case. The positive direction of the *X* axis is the starting point, 8 monitoring points counterclockwise from the *X* direction are set on each

circle, and the circumferential interval of the detection points is 45°. The monitoring circle setting is shown in Fig. 9.
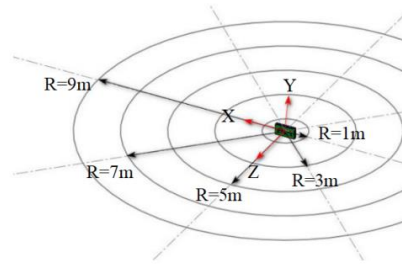

Fig. 9. Schematic diagram of the monitoring circle.

The noise directivity diagrams for the three types of blind holes and the original device when the guardrail just enters the blowing device are shown in Fig. 10. The noise directivity diagram for the original device is shown in Fig. 10(a). For the original device, the maximum value of the sound pressure level is 113.3 dB at the monitoring point of R=1 m and the direction of 90° (along the direction of the corrugated board movement), and the minimum value is approximately 63.6 dB at the 0° and 180° directions (along the width of the corrugated board) of the R=9 m monitoring circle. In the same monitoring circle, the SPL of the monitoring point in the 90° direction is the largest, and the SPL of the monitoring point in the 270° direction is the second largest. The SPL of the monitoring points at 0° and 180° are smaller than the sound pressure levels in other directions, while the sound pressure level distribution of the monitoring points in other directions is relatively even. As the monitoring radius increases, the SPL of the monitoring points in each direction gradually decreases.

The noise directivity diagram for the round hole is shown in Fig. 10(b), while Fig. 10(c) and Fig. 10(d) show those for the square hole and triangle hole, respectively. The figures show that the blowing device with blind holes on the outlet slope has sound pressure distribution rules similar to those of the original device. The maximum value of the SPL is at the monitoring point of R=1 m and the direction of 90°. For round holes, square holes and triangular holes, the sound pressure values are 99.2 dB, 102.4 dB, and 104.7 dB, respectively. The minimum value is at the 0° and 180° directions of the R=9 m monitoring circle. For round holes, square holes and triangular holes, the sound pressure values are 66.1 dB, 59.2 dB, and 59.2 dB, respectively. We found that circular holes have a better noise reduction effect along the moving direction of the corrugated board. For round holes, square holes and triangular holes, the noise reduction values reach up to 14.1 dB, 10.9 dB, and 8.6 dB, respectively.

4.3 Effect of the Porosity on the Aerodynamic Noise of the Blowing Device

According to the research in the previous section, the device with a cylindrical blind hole has the best noise
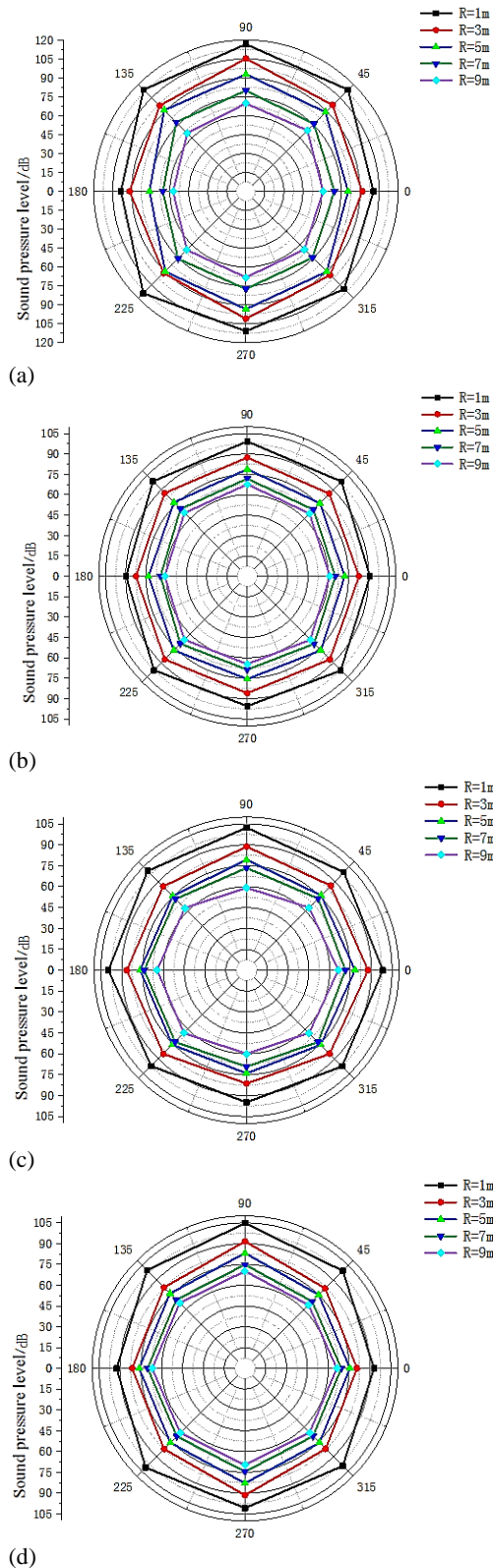
(a)

(b)

(c)

(d)

Fig. 10. Noise directivity diagram when the guardrail just enters the blowing device: (a) for the original device, (b) for the round hole, (c) for the square hole, and (d) for the triangle hole.

reduction effect when the depth and porosity of the blind holes are the same. Based on the blowing device with round holes (d=1 mm, d_h =2 mm,

$\sigma = 5\%$), the influence of porosity on aerodynamic noise is investigated. Keeping the depth (d_h =2 mm) and diameter(d=1mm) of the blind holes unchanged, three cases, for the porosity $\sigma = 10\%$, $\sigma = 15\%$ and 20%, were studied separately and compared with the original blind hole device, the porosity $\sigma = 5\%$. The parameters of the device with cylindrical blind holes are listed in Table 2.

When the guardrail board just enters the external blowing device, the sound pressure level distribution along the circumferential direction at the monitoring circle R=1m are shown in Fig. 11, for the porosity $\sigma = 5\%$, $\sigma = 10\%$, $\sigma = 15\%$ and 20%. It is shown that when the porosity is up to 10%, the noise reduction effect is the best. Compared with the original blowing device, the noise reduction is up to 23.4dB for the device with round hole and the porosity $\sigma = 10\%$. For the $\sigma = 15\%$ and$\sigma = 20\%$, the noise reduction value is up to 21.1dB, 16.9dB, respectively. We noted that when the porosity reaches 20%, tonal noise appears at 90 degrees and 270 degrees. In fact, the similar phenomenon occurs when we research the porous trailing edge Zhang and Chong (2020).

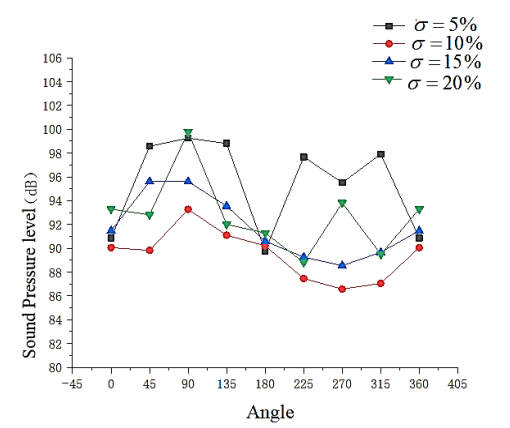**Fig. 11. Sound pressure changes with the circumferential angle when the monitoring radius is 1m, for case:$\sigma = 5\%$, $\sigma = 10\%$, $\sigma = 15\%$ and 20%.**

4.4 Effect of the Depth on Aerodynamic Noise of the Blowing Device

According to the research in the previous section, the device with the porosity $\sigma = 10\%$ has the best noise reduction effect. Based on the blowing device with round holes (d=1mm, d_h =2mm, $\sigma = 10\%$), the influence of the depth of blind holes on aerodynamic noise is investigated. Keeping the porosity ($\sigma = 10\%$) of the blind holes unchanged, four cases, d_h =1mm, d_h =2mm, d_h =3mm and d_h =4mm, were studied separately. The depth parameters of the device with cylindrical blind holes are listed in Table 3.

Noise directivity diagram at the monitoring circle of R=1 m, 3 m, 5 m, 7 m, 9 m are shown in Fig. 12 with the depth d_h =1 mm, d_h =2 mm, d_h =3 mm and d_h =4 mm. It is shown that the maximum value of the SPL is at the direction of 90°. This is similar to that of the
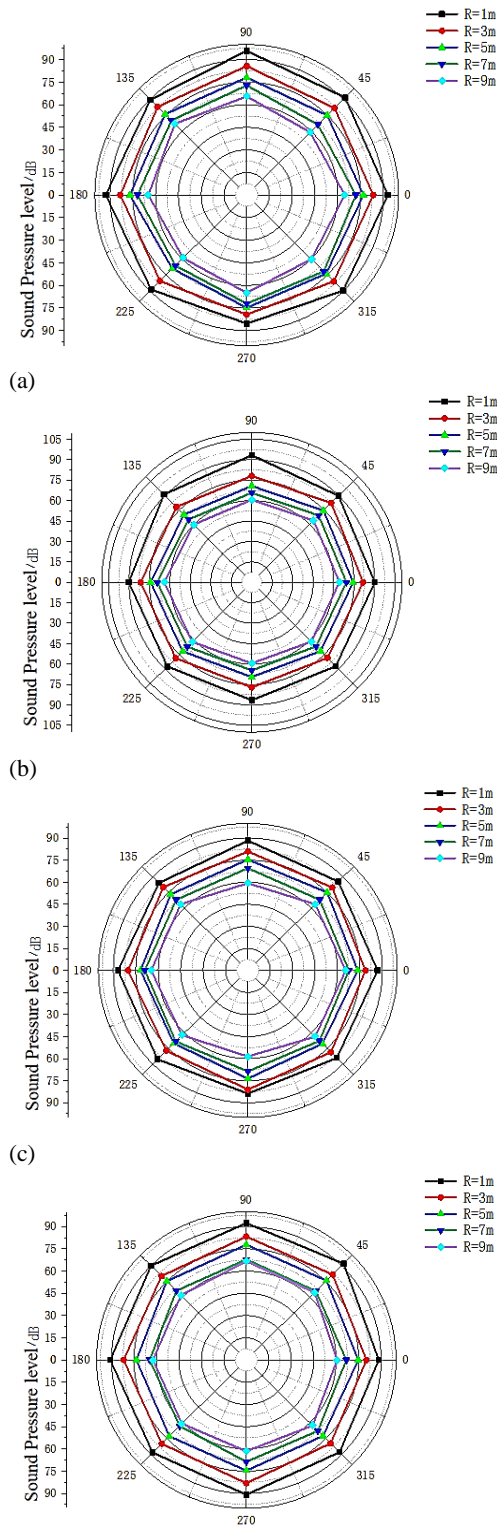
(a)

(b)

(c)

(d)

Fig. 12. Noise directivity diagram for $\sigma = 10\%$ **when the guardrail just enters the blowing device: (a)** $d_h = 1$ **mm, (b)** $d_h = 2$ **mm, (c)** $d_h = 3$ **mm, and (d)** $d_h = 4$ **mm.**

original device. Except for the monitoring points in the 90° direction, the SPL distribution of the monitoring points in the other directions is relatively uniform. This is very different from the sound pressure change of the original device along the

circumferential direction. As the radius of the monitoring circle increases, the SPL of the monitoring points in each direction gradually decreases, and the sound pressure distribution becomes more uniform. For the cases $d_h = 1$ mm, $d_h = 2$ mm, $d_h = 3$ mm and $d_h = 4$ mm, the maximum sound pressure values are 95.8 dB, 93.3 dB, 88.3 dB, and 92.3 dB, respectively, in the 90° direction of the R=1 m monitoring circle. We found that the cases where $d_h = 3$ mm have a better noise reduction effect along the moving direction of the corrugated board. For the cases of $d_h = 1$ mm, $d_h = 2$ mm, $d_h = 3$ mm and $d_h = 4$ mm with $\sigma = 10\%$, the noise reduction values reach up to 20.9 dB, 23.4 dB, 28.4 dB and 24.4 dB, respectively.

The circumferential noise value distributions of the blowing device with blind round holes for the cases $d_h = 1$ mm, $d_h = 2$ mm, $d_h = 3$ mm, and $d_h = 4$ mm are shown in Fig. 13 when the monitoring circle R= 1 m. It is shown that the noise value of the blowing device decreases first and then increases as the depth of the opening increases. When the depth of the blind holes is 3 mm, the sound pressure level value distribution in all directions is relatively uniform and reaches the minimum value. In this situation, it has the best noise reduction effects.
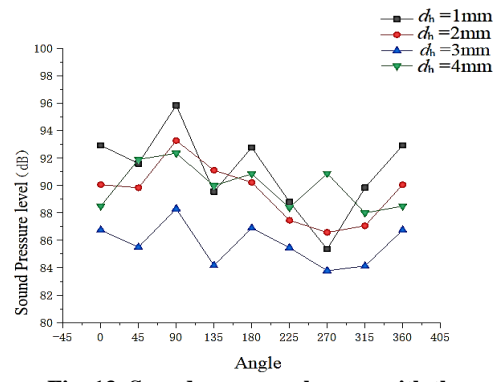

Fig. 13. Sound pressure changes with the circumferential angle when the monitoring radius is 1 m for the cases: $d_h = 1$ **mm,** $d_h = 2$ **mm,** $d_h = 3$ **mm,** $d_h = 4$ **mm.**

4.5 Analysis of the Mechanism of the Blind Hole Affecting Aerodynamic Noise

In this section, parameters such as velocity and dynamic pressure around the blow ring outlet ramp are compared to explore the noise reduction mechanism of blind holes.

The velocity distribution in the flow field is calculated when the porosity rate σ ranges from 5% to 20% with different hole shapes to study the mechanism of the blind holes affecting aerodynamic noise. The velocity distribution around the blow ring outlet ramp for the original blow ring and blind hole model with a cylinder hole and σ= 5% is shown in Fig. 14(a) and Fig. 14(b). Please note that the outlet section is selected with Z=0 mm, which is located at the mid-span plane of the blow ring. Compared with the original blow ring, the velocity distribution at the outlet is relatively uniform, and the velocity gradient
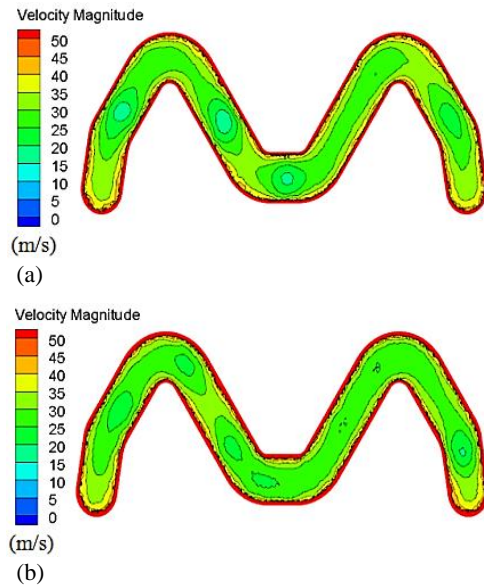
Fig. 14. Velocity contour at the air outlet of the outer blowing ring: (a) original model and (b) blind hole model.
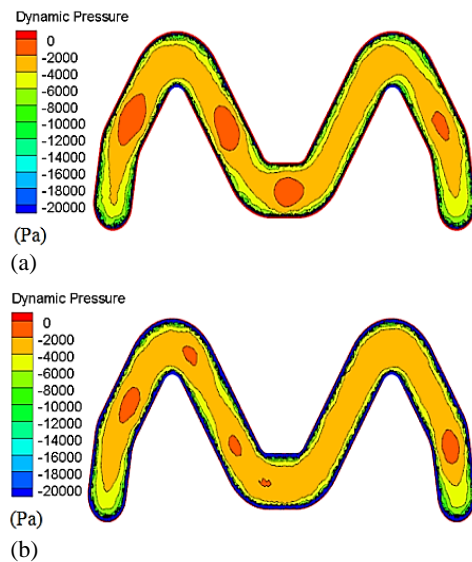

Fig. 15. Dynamic pressure contour at the air outlet of the outer blowing ring: (a) original model and (b) blind hole model.

in the center direction of the outlet decreases for the blind hole model. Therefore, the gas backflow is weakened, and the corresponding vortex is reduced, which should be the reason for the reduction in noise in the blind hole model.

The dynamic pressure distribution around the blow ring outlet ramp for the original blow ring and blind hole model with a cylinder hole and $\sigma = 5\%$ is shown in Fig. 15(a) and Fig. 15(b). It is shown that compared with the original blow ring, the dynamic pressure distribution at the outlet is relatively uniform. In general, the blind holes on the blow ring outlet ramp improve the flow performance of the blow ring so that the aerodynamic noise is reduced.

5. COLLECT AND MEASURE THE NOISE OF CERTAIN MONITORING POINTS

According to the numerical simulation analysis, the blowing device with cylindrical holes whose porosity is 10% and the hole depth is 3 mm has the best noise reduction effect. The aerodynamic noise test was carried out on the blowing device in the corrugated board galvanizing workshop to verify the correctness of the numerical simulation results. The arrangement of the experimental monitoring points is shown in Fig. 16(a). The black dots in the figure are the locations of the monitoring points. The positive direction of the X-axis is the starting point in each monitoring circle. Limited by the space structure of the galvanizing site, 6 monitoring points are arranged for the same device. Monitoring points 1, 2, and 3 are located at 0°, 90°, and 180° of the monitoring circle with R=1 m. Monitoring points 4, 5, and 6 are located at 0°, 90°, and 180° of the monitoring circle with R=5 m. PCB microphones with a sensitivity of 55.53 mV/Pa, a dynamic range of 20~140 dB, and a frequency range of 20 Hz~20 kHz are used in the experiments. The microphones are fixed on the bracket. The details and installation of the microphone are shown in Fig. 16(b).
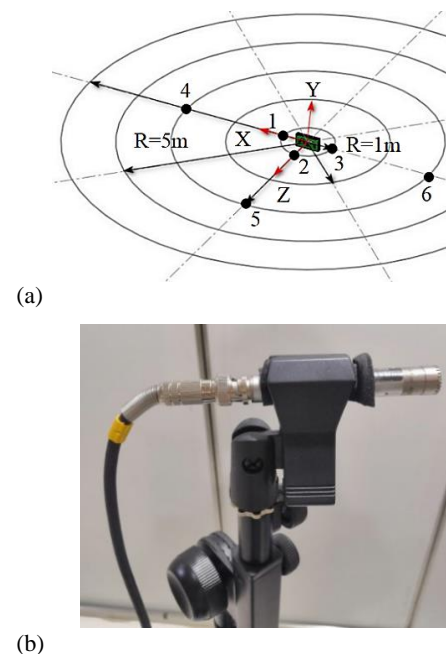

(a)

(b)

Fig. 16. (a) Arrangement of the experimental monitoring points and (b) PCB microphone and installation method.

The comparison between the experimental noise data and the numerical simulation data of each monitoring point when the guardrail just enters the blowing device is shown in Table 5. It is shown that the agreement between the numerical and experimental results is acceptable. However, the experimental noise values are greater than the simulation results. This is because the experimentally measured noise is the result of the superposition of the background noise of the corrugated board galvanizing workshop

Table 5 Comparison between the experimental noise data and the numerical simulation data of each monitoring point

monitoring point	Original device		Optimal device	
	Experimental	Numerical simulation	Experimental	Numerical simulation
1	102.12	100.64	92.65	86.75
2	119.14	116.69	96.05	88.30
3	100.03	98.55	92.76	86.89
4	80.57	78.82	79.39	73.41
5	95.11	92.88	82.67	75.45
6	78.28	76.09	71.81	69.19

and the aerodynamic noise generated by the blowing device. The noise at monitoring point 90° in each monitoring circle is obviously larger than those in other directions, which is similar to the numerical simulation results.

6. CONCLUSION

To solve the problem of the strong noise generated in the galvanizing process on the surface of guardrail boards, the flow field and sound field of the blowing device of guardrail boards are analyzed using dynamic grid technology. Based on the results of numerical analysis and the mechanism of aerodynamic noise, optimal design of the outlet structure of the blowing device is carried out according to the sound absorption and noise reduction theory of microperforated plates. The oblique surface of the outlet is processed with blind holes to explore the influence of blind holes on the aerodynamic noise of the blowing device, including different shapes, different porosities and different depths. In addition, an aerodynamic noise test was carried out on the blowing device in the corrugated board galvanizing workshop to verify the correctness of the numerical simulation results. The key findings of this paper are listed as follows:

(1) The place with the largest noise sound pressure level is at the outlet of the blowing device, and the value of the sound pressure level is 113.3 dB at the monitoring point of R=1 m and the direction of 90°. The SPLs of the monitoring points at 0° and 180° are smaller than the SPLs in other directions, while the SPL distribution of the monitoring points in other directions is relatively even. As the monitoring radius increases, the SPL of the monitoring points in each direction gradually decreases. When the guardrail board just enters the blowing device, there is greater noise at the outlet than in other working conditions.

(2) The blowing device with blind holes on the outlet slope has sound pressure distribution rules similar to those of the original device. The maximum value of the SPL is at the monitoring point of R=1 m and the direction of 90°. For round holes, square holes and triangular holes, the maximum SPL values are 99.2 dB, 102.4 dB, and 104.7 dB, and the noise reduction values reach 14.1 dB, 10.9 dB, and 8.6 dB, respectively. The circular holes have a better noise reduction effect.

(3) Compared with the original blowing device, the noise reduction reaches up to 23.4 dB for the device with a round hole and porosity $\sigma = 10\%$. For $\sigma = 15\%$ and $\sigma = 20\%$, the noise reduction values are reach to 21.1 dB and 16.9 dB, respectively. We noted that when the porosity reaches 20%, tonal noise appears at 90° and 270°. When the porosity reaches 10%, the noise reduction effect is better.

(4) For the cases $d_h = 1$ mm, $d_h = 2$ mm, $d_h = 3$ mm and $d_h = 4$ mm, the maximum sound pressure values are 95.8 dB, 93.3 dB, 88.3 dB, and 92.3 dB at the 90° direction of the R=1 m monitoring circle, and the noise reduction values reach up to 20.9 dB, 23.4 dB, 28.4 dB and 24.4 dB, respectively. The cases where $d_h = 3$ mm have a better noise reduction effect.

(5) The blowing device with cylindrical holes with a porosity of 10% and a hole depth of 3 mm has the best noise reduction effect.

DATA AVAILABILITY STATEMENT

The data that support the findings of this study are available from the corresponding author upon reasonable request.

CONFLICTS OF INTEREST

The author(s) declare no potential conflicts of interest with respect to the research, authorship, and/or publication of this article.

FUNDING STATEMENT

REFERENCES

Anyoji, M. and I. Tabaru (2017). Effect of boundary layer trip on reduction of jet noise in over-expanded nozzle flow. *Journal of Thermal Science* 26(5), 448-452.

Barbarino, M., M. Ilsami, R. Tuccillo and L. Federico (2017). Combined CFD-Stochastic analysis of an active fluidic injection system for

jet noise reduction. *Applied Sciences* 7(623), 1-17.

Baqui, Y. B., A. Agarwal1, A. V. G. Cavalieri and S. Sinayoko (2015). A coherence-matched linear source mechanism for subsonic jet noise. *Journal Fluid Mechanics* 776, 235–267.

Baskaran, K., S. K. Parimalanathan, A. Dhamanekar and K. Srinivasan (2018). Effects of passive grids on pipe and orifice jet noise. *Journal of Sound and Vibration* 435, 218–233.

Bychkova, O. P. and G. A. Faranosov (2014). On the possible mechanism of the jet noise intensification near a wing. *Acoustical Physics* 60(6), 633–646.

Balakrishnan, P. and K. Srinivasan (2019). Impinging jet noise reduction using non-circular jets. *Applied Acoustics* 143, 19–30.

Brehma, C., J. A. Housmanb, C. C. Kiris, M. F. Baradb and F. V. Hutcheson (2017). Four-jet impingement: Noise characteristics and simplified acoustic model. *International Journal of Heat and Fluid Flow* 67, 43–58.

Balakrishnan, P. and K. Srinivasan (2017). Pipe jet noise reduction using co-axial swirl pipe. *The Aeronautical Journal* 121(1238), 488-514.

Dahl, M. D. (2015). Turbulence statistics for jet noise source modeling from filtered PIV measurements. *Aeroacoustics* 14 (3-4), 521 – 552.

Doty, M. J., T. F. Brooks, C. L. Burley, C. J. Bahr and D. S. Pope (2018). Jet noise shielding provided by a hybrid wing body aircraft. *International Journal of Aeroacoustics* 17(1–2), 135–158.

Faranosov, G. and I. Belyaev (2019). Azimuthal structure of low-frequency noise of installed jet. *AIAA Journal* 57(5), 1885-1898.

Ilário, C. R. S., M. Azarpeyvand, V. Rosa, R. H. Self and J. R. Meneghini (2017). Prediction of jet mixing noise with lighthill's acoustic analogy and geometrical acoustics. *The Journal of the Acoustical Society of America* 141(2), 1203-1213.

Karabasov, S. A. and R. D. Sandberg (2015). Influence of free stream effects on jet noise generation and propagation within the Goldstein acoustic analogy approach for fully turbulent jet inflow boundary conditions. *Aeroacoustics* 14 (3-4), 413 – 430.

Koenig, M., K. Sasaki, A. V. G. Cavalieri, P. Jordan and Y. Gervais (2016). Jet-noise control by flfluidic injection from arotating plug: linear and nonlinearsound-source mechanisms. *Journal Fluid Mechanics* 788, 358–380.

Lee, H., A. Uzun and M. Y. Hussaini (2017). Identification of jet noise source using causality method based on large-eddy simulation of a round jet flow. *International Journal of Aeroacoustics* 16(1–2), 78–96.

Liu, G. Q., T. Zhang, Y. O. Zhang and X. Li (2014). Underwater jet noise simulation based on a Large-Eddy Simulation/Lighthill hybrid method. *168th Meeting of the Acoustical Society of America, 27-31 October, Indianapolis, Indiana*, Vol. 22 070005.

Liu, J. T. C. (2016). Some fundamental considerations of streamwise vortices found useful in mixing enhancement and jet noise suppression. *International Journal of Aeroacoustics* 15(4–5), 515–525.

Lee, I., Y. Z. Zhang and D. K. Lin (2019). Experimental investigation of jet noise from a high BPR dual-stream jet in a static model-scale test. *Applied Acoustics* 150, 246–267.

Nelson, C. C., A. B. Cain, R. Dougherty, K. S. Brentner and P. J. Morris (2017). Application of synthetic array techniques for improved simulations of hot supersonic jet noise. *International Journal of Aeroacoustics* 16(4–5), 382–402.

Pouangué, A. F., M. Sanjosé and S. Moreau (2015). Subsonic jet noise simulations using both structured and unstructured grids. *AIAA Journal* 53(1), 55-69.

Pankaj, R. and K. Sunil (2019). Use of downstream fluid injection to reduce subsonic jet noise. *International Journal of Aeroacoustics* 18(4-5), 554–574.

Pilon, A. R., R. W. Powers, D. K. McLaughlin and P. J. Morris (2017). Design and analysis of a supersonic jet noise reduction concept. *Journal of Aircraft* 54(5),1705-1717.

Semiletov, V. A. and S. A. Karabasov (2017). Similarity scaling of jet noise sources for low-order jet noise modelling based on the Goldstein generalised acoustic analogy. *International Journal of Aeroacoustics* 16(6), 476–490.

Semiletov, V. A., P. G. Yakovlev, S. A. Karabasov, G. A. Faranosov and V. F. Kopiev (2016). Jet and jet–wing noise modelling based on the CABARET MILES flow solver and the Ffowcs Williams–Hawkings method. *International Journal of Aeroacoustics* 15(6–7), 631–645.

Shur, M. L., P. R. Spalart and M. K. Strelets (2016). Jet noise computation based on enhanced DES formulations accelerating the RANS-to-LES transition in free shear layers. *International Journal of Aeroacoustics* 15(6–7), 595–613.

Tester, B. J. and S. Glegg (2018). Phased array transformation methods to estimate non-compact jet noise source characteristics. *International Journal of Aeroacoustics* 17(4–5), 380–398.

Viswanathan, K. (2018). Progress in prediction of jet noise and quantification of aircraft/engine noise components. *International Journal of Aeroacoustics* 17(4–5), 339–379.

.

Wei, X. F., R. Mariani, L. P. Chua, H. D. Lim, Z. B. Lu, Y. D. Cui and T. H. New (2019). Mitigation of under-expanded supersonic jet noise through stepped nozzles. *Journal of Sound and Vibration* 459, 114875.

Zhang, M. H. and T. P. Chong (2020). Effects of porous trailing edge on aerodynamic noise characteristics. International Journal of Aeroacoustics 19(3–5), 254–271.